

## Diffusive separation in rarefied plume interaction

Vesper, J. Elin; Kenjereš, Saša; Kleijn, Chris R.

**DOI**

[10.1116/6.0002126](https://doi.org/10.1116/6.0002126)

**Publication date**

2022

**Document Version**

Final published version

**Published in**

Journal of Vacuum Science and Technology B

**Citation (APA)**

Vesper, J. E., Kenjereš, S., & Kleijn, C. R. (2022). Diffusive separation in rarefied plume interaction. *Journal of Vacuum Science and Technology B*, 40(6), Article 064202. <https://doi.org/10.1116/6.0002126>

**Important note**

To cite this publication, please use the final published version (if applicable).  
Please check the document version above.

**Copyright**

Other than for strictly personal use, it is not permitted to download, forward or distribute the text or part of it, without the consent of the author(s) and/or copyright holder(s), unless the work is under an open content license such as Creative Commons.

**Takedown policy**

Please contact us and provide details if you believe this document breaches copyrights.  
We will remove access to the work immediately and investigate your claim.

***Green Open Access added to TU Delft Institutional Repository***

***'You share, we take care!' - Taverne project***

***<https://www.openaccess.nl/en/you-share-we-take-care>***

Otherwise as indicated in the copyright section: the publisher is the copyright holder of this work and the author uses the Dutch legislation to make this work public.

# Diffusive separation in rarefied plume interaction <sup>EP</sup>

Cite as: J. Vac. Sci. Technol. B **40**, 064202 (2022); <https://doi.org/10.1116/6.0002126>

Submitted: 28 July 2022 • Accepted: 14 September 2022 • Published Online: 07 November 2022

 J. Elin Vesper, Saša Kenjereš and  Chris R. Kleijn

## COLLECTIONS

 This paper was selected as an Editor's Pick



View Online



Export Citation




CrossMark

## ARTICLES YOU MAY BE INTERESTED IN


[On the nonlinear thermal stress, thermal creep, and thermal edge flows in triangular cavities](#)  
Physics of Fluids **34**, 052002 (2022); <https://doi.org/10.1063/5.0088539>

[Thermodynamically admissible 13-moment equations](#)  
Physics of Fluids **34**, 017105 (2022); <https://doi.org/10.1063/5.0078780>

[A simple hydrodynamic-particle method for supersonic rarefied flows](#)  
Physics of Fluids **34**, 057101 (2022); <https://doi.org/10.1063/5.0088946>



**HIDEN**  
ANALYTICAL



40 YEARS  
1982 - 2022


# Instruments for Advanced Science

- Knowledge,
- Experience,
- Expertise

Click to view our product catalogue


Contact Hiden Analytical for further details:  
[www.HidenAnalytical.com](http://www.HidenAnalytical.com)  
[info@hideninc.com](mailto:info@hideninc.com)

Gas Analysis




- ▶ dynamic measurement of reaction gas streams
- ▶ catalysis and thermal analysis
- ▶ molecular beam studies
- ▶ dissolved species probes
- ▶ fermentation, environmental and ecological studies

Surface Science




- ▶ UHVTPD
- ▶ SIMS
- ▶ end point detection in ion beam etch
- ▶ elemental imaging - surface mapping

Plasma Diagnostics



- ▶ plasma source characterization
- ▶ etch and deposition process reaction kinetic studies
- ▶ analysis of neutral and radical species

Vacuum Analysis



- ▶ partial pressure measurement and control of process gases
- ▶ reactive sputter process control
- ▶ vacuum diagnostics
- ▶ vacuum coating process monitoring

# Diffusive separation in rarefied plume interaction

Cite as: J. Vac. Sci. Technol. B **40**, 064202 (2022); doi: [10.1116/6.0002126](https://doi.org/10.1116/6.0002126)

Submitted: 28 July 2022 · Accepted: 14 September 2022 ·

Published Online: 7 November 2022



J. Elin Vesper,<sup>1,2,a)</sup>  Saša Kenjereš,<sup>1,2</sup> and Chris R. Kleijn<sup>1,2</sup> 

## AFFILIATIONS

<sup>1</sup>Department of Chemical Engineering, Faculty of Applied Sciences, Delft University of Technology, van der Maasweg 9, 2629 HZ Delft, The Netherlands

<sup>2</sup>J.M. Burgerscentrum for Fluid Mechanics, Mekelweg 2, 2628 CD Delft, The Netherlands

<sup>a)</sup>Electronic mail: [j.e.vesper@tudelft.nl](mailto:j.e.vesper@tudelft.nl)

## ABSTRACT

In the present study, we propose the use of a light, inert carrier gas to support deposition uniformity and rate in continuous physical vapor deposition, in which closely spaced slots or nozzles are required to achieve a sufficiently high deposition rate. Interaction shocks between the emerging rarefied plumes cause undesired nonuniformities in the deposited coating. The present work evaluates the effect of adding a carrier gas on the interaction shock. We study the interaction between two sonic plumes consisting of a binary mixture, i.e., silver as coating material and helium as a light inert carrier gas, by direct simulation Monte Carlo. While the inlet Mach and Knudsen numbers were kept constant, the fraction of carrier gas was varied to single out the effect of species separation. The influence of rarefaction on species separation was also studied. Species separation produces a high carrier-gas fraction in the periphery and an accumulation of the heavier species in the jet core. The resulting change in the speed of sound alters the local expansion characteristics and, thus, shifts the shock location and weakens the shock. These phenomena intensify with the degree of rarefaction. It is shown that adding a light carrier gas increases deposition rate may enhance uniformity and reduce stray deposition.

Published under an exclusive license by the AVS. <https://doi.org/10.1116/6.0002126>

## I. INTRODUCTION

In thin-film deposition processes from the gas phase, such as physical vapor deposition (PVD), varying the inert and reactive gas mixture composition is used to influence the layer growth mode,<sup>1</sup> enhance uniformity,<sup>2</sup> or to produce compounds, such as titanium nitride, which requires a nitrogen atmosphere.<sup>3</sup> Several experimental and numerical studies analyzed the effect of adding an inert background or carrier gas onto the film thickness and distribution in batch deposition processes, mainly finding a smoothing of the deposition profile and a decrease of deposition rate due to an enhanced number of collisions.<sup>2,4–7</sup> Directed vapor deposition processes<sup>8,9</sup> were developed, which utilize light carrier gases to enhance the deposition rate and reduce deposition loss (i.e., fraction of evaporated material not being deposited on the substrate). The latter diminishes production downtimes due to cleaning and maintenance in continuous lines. Inert carrier gases were used to foster the transport of coating material to undercuts since otherwise PVD is a line-in-sight technology.<sup>10–12</sup> In chemical deposition processes, carrier gases are utilized to suppress early reactions and control the reactant ratio to achieve the desired morphology of the deposited film.<sup>1</sup> It was shown that light carrier gases benefit the conductance of material through pipes and orifices and, thus, the

possible deposition rate.<sup>13,14</sup> In summary, the use of background and carrier gases decisively influences the film's growth in thin-film and coating technology.

Recently, continuous PVD lines were introduced which overcome the disadvantages of batch processes, i.e., a low deposition rate and production downtimes due to maintenance. A sufficient evaporation rate for coatings is typically reached via a thermal source,<sup>15</sup> whereas maintenance is reduced by avoiding stray deposition using plumes (or jets) directed toward the substrate emerging from multiple closely spaced nozzles or slots.<sup>16,17</sup> In these plume clusters, the initially free expansion interacts with neighboring plumes producing shocks.<sup>18</sup> This causes mass flow nonuniformities, which are especially undesirable in thin-film deposition.<sup>19,20</sup> The higher the mass flow rate and the smaller the nozzle-to-nozzle distance, the higher the peaks in deposition. However, a high and uniform deposition is required in continuous coating technology to keep the coating process step at the general line speed and to obtain a high-quality coating.

The successful use of adding light carrier gases to heavy reactant gases in batch PVD and other coating processes indicates a good chance that this may also improve continuous PVD processes.

An important effect to be taken into account when utilizing mixtures of heavy and light gases is the spatial separation of the various species. This may be caused by various physical mechanisms, such as differences in body forces in centrifugal flows,<sup>21–23</sup> thermodiffusion effects in nonisothermal flows,<sup>24,25</sup> and pressure gradients in confined microflows.<sup>26,27</sup> Gas species separation occurs in microelectromechanical systems,<sup>28,29</sup> radiometric pumps,<sup>30,31</sup> Knudsen pumps,<sup>32,33</sup> and aerospace applications.<sup>34–36</sup> For the latter, pressure-driven species separation has a severe influence since both high pressure gradients and long mean free paths occur, and the separation increases with both.

Because of its relevance to aerospace applications in for instance (micro)thrusters, free expansions of rarefied plumes or jets have been comprehensively studied. Several analytical,<sup>37</sup> experimental,<sup>34,38,39</sup> and numerical<sup>13,40,41</sup> studies on multispecies gas plumes found that the heavier species accumulates around the jet axis. In contrast, the fraction of the lighter species is high in the backflow region and regions farther away from the jet axis. Simulations of species separation of an argon-helium mixture at small Knudsen numbers were performed by Riabov.<sup>40</sup> He found that the decoupling of the streamwise and the circumferential temperatures, the so-called “freezing,” which is an indication for continuum breakdown, takes place further upstream for the heavier species. Wu *et al.* studied experimentally and numerically the interaction of two three-dimensional hydrogen–oxygen thrusters at small separation distances with a focus on the interaction shock and its possible effect on a backflow.<sup>42</sup> The latter may damage the spacecraft using multiple thrusters. The effect of species separation on the flow field was not in the focus of the study.

Species separation effects are also reported for flows involving shocks, but it is difficult to establish the same generality as for free expansion flows due to the multitude of possible geometries and shock types. Rothe<sup>43</sup> experimentally studied the species separation effect in bow shocks. He found an earlier number density increase for the lighter species than the heavier one, which implies a staggered onset of the shock. Ramos *et al.*<sup>39</sup> analyzed this separation of species for a nitrogen-hydrogen mixture in supersonic jets with and without a shock-wave structure. In the former case, the authors found a steep increase of the heavier species in the jet core right after the nozzle where the pressure gradient is highest. In the shock-wave structure, Ramos *et al.*<sup>44</sup> found separation across the shocks (yielding an accumulation of lighter species slightly before and inside the Mach and Barrel shock). Additionally, background gas penetrated into the jet core after the first Mach disk, which was increased for light background gas. The authors also addressed the rotational-translational energy transfer as well as the energy transfer between species.

In summary, there exists a good understanding in the literature of species separation in free expansions of a single rarefied plume. However, the knowledge of the influence of shocks on species separation as available in the literature is limited to some specific, generally nonrarefied, gas flow configurations. To the authors’ best knowledge, species separation in interacting free expansion rarefied gas plumes with downstream interaction shocks, as it appears in plume clusters of a continuous PVD line, has not been described in the literature.

The present paper studies the species separation in planar plume interaction of a binary mixture of silver and helium and its impact on

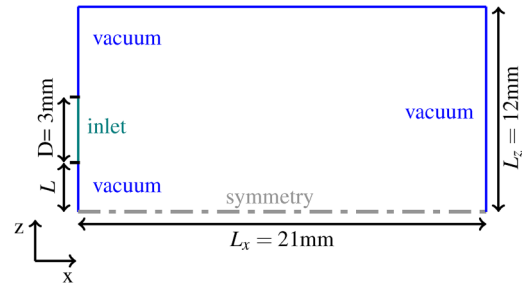


FIG. 1. Geometry and boundary conditions for the DSMC simulation.

the location and strength of the shock. We aim to answer the question how the mutual influence between shocks and species separation has an impact on mass flux magnitude and uniformity. We show how the addition of a light carrier gas influences this mutual interaction and, consequently, the deposition rate, deposition uniformity, and deposition loss. The involved phenomena are unraveled, on the one hand, by considering the free molecular flow to evaluate species separation effects and, on the other hand, by visualizing the flow field plotting the characteristic curves. With the latter also, the downstream shift of the shock location and the weakening of the shock with helium fraction and degree of rarefaction is presented.

## II. METHODS

We simulate the interaction between two parallel, planar sonic plumes by the direct simulation Monte Carlo (DSMC) method.<sup>45</sup> The plumes emerge from two inlet slots of width  $D = 3$  mm at a separation distance  $2L = 6$  mm (the distance between the edges of the nozzles, see Fig. 1). Due to the symmetry, we simulate only the upper half of the geometry. The computational domain is planar and spans  $21 \times 12$  mm<sup>2</sup>. Except for the inlet and the symmetry plane, all other boundaries are vacuum boundary conditions. The inlet mixture composition at the orifice is assumed to be uniform. The mass ratio of silver and helium is  $m_{\text{Ag}}/m_{\text{He}} = 26.94$ . At the inlet, a free stream boundary condition is applied with a mixture of silver and helium at a temperature of  $T_{\text{in}} = 2000$  K at a velocity corresponding to  $M = 1$ , which corresponds to a stagnation temperature of  $T_s = 2600$  K. The inlet density depends on the Knudsen number, which was chosen as a multiplicity of  $Kn_0 = 0.0125$ , i.e.,  $Kn \in [Kn_0, 2Kn_0]$ , and the carrier-gas fraction, i.e., the mole fraction of helium, which takes the following values  $y_{\text{He}} \in [0, 0.1, 0.3, 0.5, 0.7, 0.9, 1]$ . The inlet velocity is the speed of sound, which depends on the mixture composition. To determine the inlet number density from the inlet Knudsen number  $Kn_{\text{in}} = \lambda/D$ , the mean free path of the binary mixture needs to be evaluated as<sup>45</sup>

$$\lambda = \frac{1}{n\pi} \left[ \frac{y_{\text{He}}}{\sqrt{2}d_{\text{He}}^2 y_{\text{He}} + \sqrt{1 + \frac{m_{\text{He}}}{m_{\text{Ag}}} d_{\text{He,Ag}}^2 y_{\text{Ag}}}} + \frac{1 - y_{\text{He}}}{\sqrt{1 + \frac{m_{\text{Ag}}}{m_{\text{He}}} d_{\text{He,Ag}}^2 y_{\text{He}} + \sqrt{2}d_{\text{Ag}}^2 y_{\text{Ag}}}} \right], \quad (1)$$

where the collisional diameter for each species varies with temperature according to the variable hard sphere model<sup>45</sup> as follows:

$$d = d_{ref} \left( \frac{T_{ref}}{T_{in}} \right)^{\left( \frac{\omega}{2} - \frac{1}{4} \right)}, \quad (2)$$

where the energy exponent  $\omega$  and reference diameter  $d_{ref}$  are given in Table I. The collisional diameter between atoms of different species is given as

$$d_{He,Ag} = \frac{1}{2} (d_{He} + d_{Ag}). \quad (3)$$

The inlet speed, i.e., the speed of sound of the mixture, is given by

$$a = \sqrt{\gamma \frac{k_B T_{in}}{(y_{He} m_{He} + (1 - y_{He}) m_{Ag})}}. \quad (4)$$

DSMC requires a thermodynamic closure for the collisions to match the macroscopic transport properties. For this, the variable soft sphere model<sup>45</sup> is applied, since the viscosity and binary diffusivity cannot be correctly modeled by simpler models. The properties of helium and silver are listed in Table I. The reference diameter and viscosity parameter of silver are estimated by the inverse-power-law approximation described by Fan *et al.*<sup>47</sup> The reference metal for the inverse-power law was rubidium, which is in the same group as silver and whose viscosity is reported in the literature.<sup>48</sup> The data for helium are the ones reported by Bird.<sup>45</sup> To obtain accurate results despite the decoupling applied in DSMC, a time step smaller than one-tenth of the mean collisional time has to be maintained, i.e.,  $dt < \tau/10$ , and a cell size smaller than one-third of the local mean free path is required. Since we use eight subcells per cell,<sup>49</sup> this requirement can be loosened to ( $dx < 2\lambda/3$ ). To have enough unbiased collision partners, at least 20 representative particles are required per cell. All these requirements were fulfilled, except for the highly rarefied region (i.e., in the “blind spot” of the plume where the collision probability is low anyway), which justifies our approach. To fulfill the spatial resolution criteria, first a simulation on a coarse grid was performed and based on the local mean free path refined before starting the actual simulation. The time step was also adapted and kept constant throughout the simulation. This procedure was conducted for each case, as the resolution requirements differ depending on both Knudsen number and carrier-gas fraction. The *dsmcFoamPlus* solver was used, which was implemented in *OpenFoam 2.4* and extensively verified by White *et al.*<sup>50</sup>

**TABLE I.** Modeling parameters for variable soft sphere (Ref. 46), a model for helium (Ref. 45), and silver [approximated by inverse-power law (Ref. 47)].

	$m$ ( $10^{-27}$ kg)	$d_{ref}$ ( $10^{-10}$ m)	$\omega$	$\alpha$	$T_{ref}$ (K)
He	6.65	2.3	0.66	1.26	273
Ag	179.12	8.31	0.853	1.92	273

### III. RESULTS

Three main criteria regarding mass flow are desirable in coating technology: (i) a high total deposition rate, (ii) a uniform deposition, and (iii) an avoidance of stray deposition. We use the deposition profiles of silver, i.e.,  $\dot{n}_{Ag}$ , to comprehensively quantify these criteria depending on the mixture composition. First, we evaluate (i) the total deposition rate by plotting the inlet number density fluxes over the carrier-gas fraction  $y_{He}$  for  $Kn_{in} = Kn_0$  and  $Kn_{in} = 2Kn_0$  as shown in Fig. 2. With increasing carrier-gas fraction, the silver mass flux—which we are eventually interested in—rises up to its maximum at  $y_{He} = 0.755$ . This increase may seem counterintuitive, since the silver fraction decreases with a higher helium fraction. Nevertheless, the silver inlet velocity increases, since the speed of sound is inversely proportional to the square root of molecular mass, i.e.,  $a \propto 1/\sqrt{m}$ . It should be noted that the addition of a lighter carrier gas increases viscosity with  $1/\sqrt{m}$ , which may increase the boundary layer in the slot or nozzle and, thus, reduce the outflow. The present study does not consider this effect. Comprehensive studies on the conductance and species separation from orifices and through pipes of finite lengths were published in recent years.<sup>13,14,51</sup> However, as the higher viscosity affects only the boundary and not the bulk flow, the effect is assumed to be small.

To quantify (ii) the uniformity of the deposition, the minimum squared deviation of silver deposition (i.e., minimized with respect to  $c$ , a number from the set of real numbers) is calculated, which reads

$$A_{dev} = \min_{c \in \mathbb{R}^+} \int_{z=0}^{z=12 \text{ mm}} \left( \frac{\dot{n}_{Ag} - c}{c} \right)^2 dz. \quad (5)$$

$A_{dev} = 0$  corresponds to perfect uniformity, whereas higher  $A_{dev}$  indicates nonuniformity. Figures 3(a) (for  $Kn = Kn_0$ ) and 3(b) (for  $Kn = 2Kn_0$ ) show the nonuniformity measure  $A_{dev}$  over the nozzle-to-plate distance and molar fraction of helium  $y_{He}$ . The nonuniformity is highest directly after the inlet, where the spreading of species starts, and decreases rapidly with increasing distance. The nonuniformity starts to differ for different molar

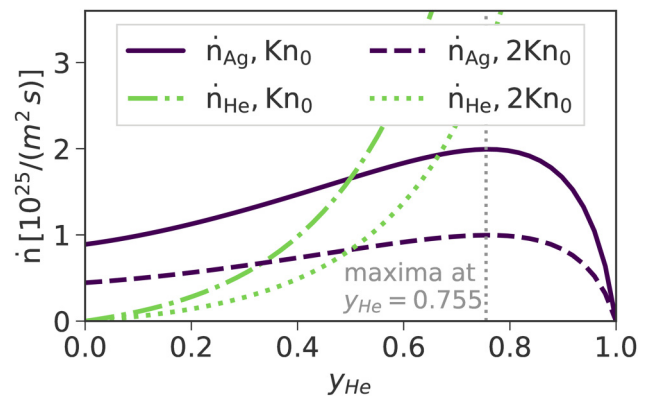


**FIG. 2.** Inlet number density fluxes depending on carrier-gas fraction.

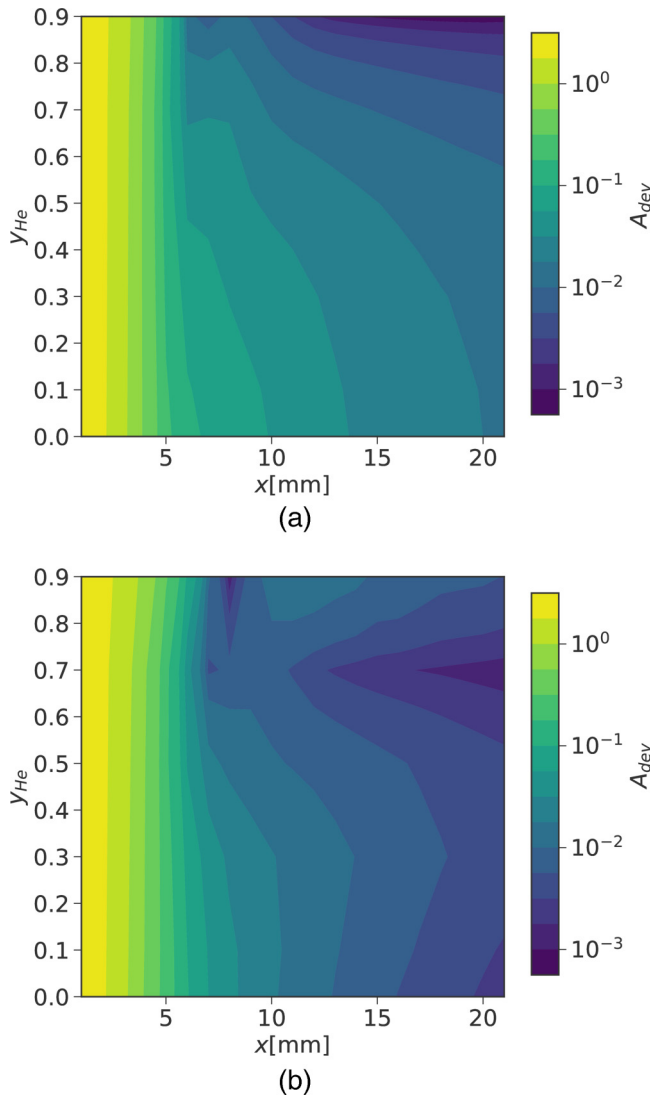


**FIG. 3.** Nonuniformity  $A_{dev}$  depending on carrier-gas fraction and nozzle-to-plate distances for two plumes at a nozzle separation distance  $L = D$  for (a)  $Kn = Kn_0$  and (b)  $Kn = 2Kn_0$ .

fractions of helium at a nozzle-to-plate distance of  $x \approx 5$  mm. For  $Kn = Kn_0$ , adding more carrier gas monotonically enhances uniformity, whereas for  $Kn = 2Kn_0$ , the nonuniformity decreases up to a minimum approximately at  $y_{He} = 0.7$  before increasing again. While the exact minimum value can be expected to depend on the geometry and process conditions, it indicates that high fractions of carrier gas may mitigate shock-induced nonuniformities. Figures 4(a) and 4(b) show (iii) the stray deposition, which is the coating material fraction  $p_{loss}$  that does not reach the substrate (assumed to stretch over the range  $z = \pm 12$  mm) but leaves the computational domain (i.e., coats the vacuum chamber). With a higher nozzle-to-plate distance, the loss deposition increases. The

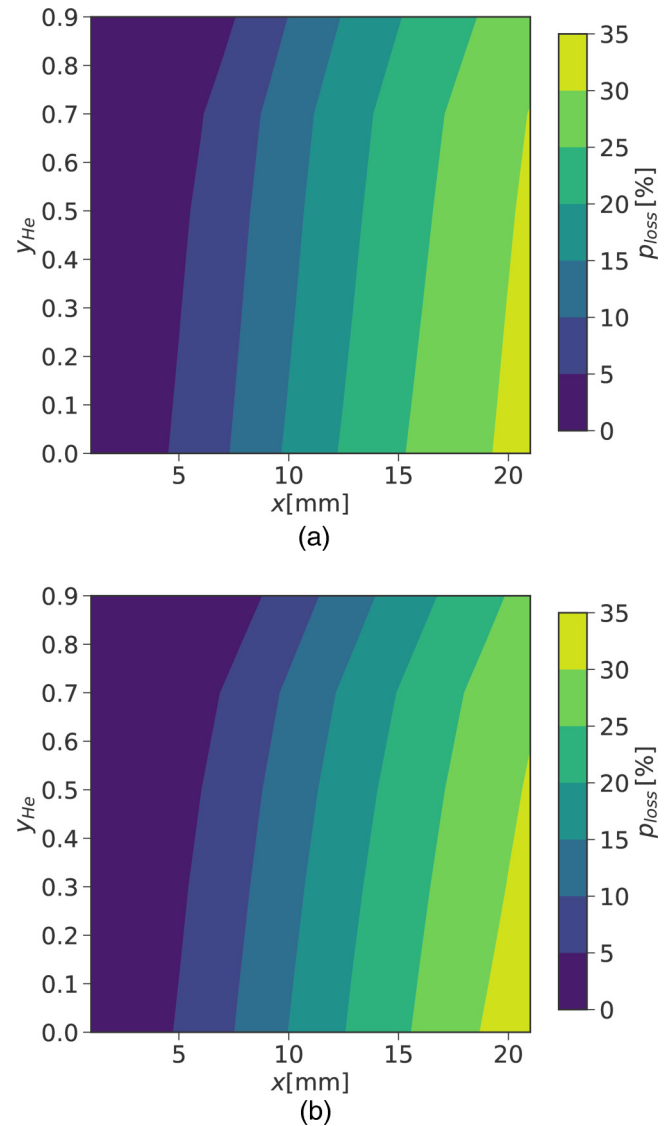


**FIG. 4.** Stray deposition loss  $p_{loss}$  depending on carrier-gas fraction and nozzle-to-plate distances for two plumes at a nozzle separation distance  $L = D$  for (a)  $Kn = Kn_0$  and (b)  $Kn = 2Kn_0$ .

stray deposition loss is slightly higher for  $Kn = Kn_0$  [Fig. 4(a)] than for  $Kn = 2Kn_0$  [Fig. 4(b)]. The higher the carrier-gas fraction, the smaller the deposition loss, e.g., at  $x = 10$  mm only 10% are lost for  $y_{He} = 0.9$  compared to 15% for no carrier gas for the case of  $Kn = 2Kn_0$  [Fig. 4(b)]. Thus, adding a light carrier gas improves the coating deposition regarding all three evaluated criteria.

To explain these results, Fig. 5 shows the line profiles of the normalized silver number density, silver velocity, and normalized silver deposition along  $z$ -direction for different mole fractions of



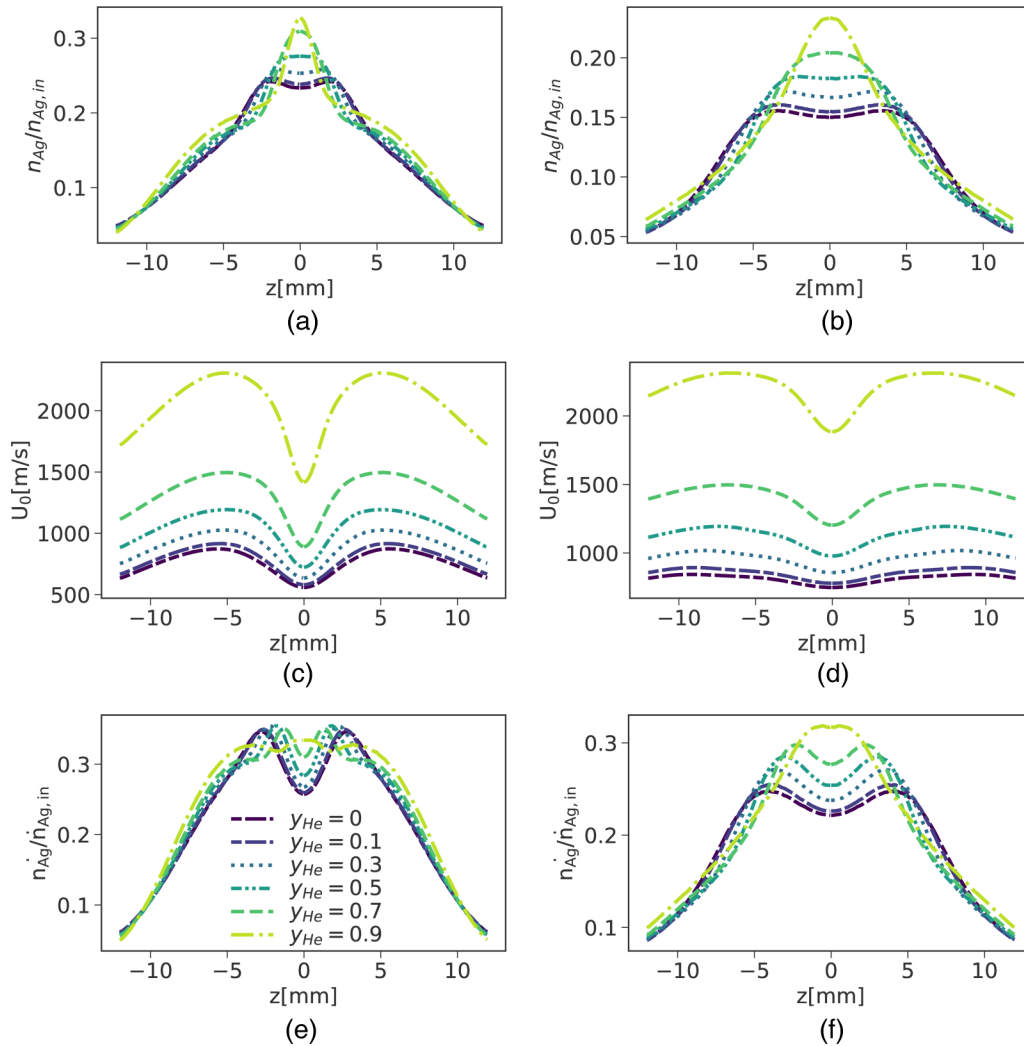


**FIG. 5.** Line profiles of the flow of two interacting plumes for  $Kn = 2Kn_0$  and for several carrier-gas fractions along  $z$ -direction. (a) and (b) show the silver number density normalized by the silver inlet number density, (c) and (d) the silver velocity in  $x$ -direction, and (e) and (f) the silver number density flux normalized by the silver inlet number density flux. (a), (c), and (e) are at a nozzle-to-plate distance of  $x = 8$  mm and (b), (d), and (f) at a nozzle-to-plate distance of  $x = 15$  mm.

carrier gas  $y_{He}$  for  $Kn = 2Kn_0$ . At  $x = 8$  mm, the normalized number density profile for the pure silver mixture, i.e.,  $y_{He} = 0$  [Fig. 5(a)], linearly increases toward the symmetry and shows two elevated peaks on each side of the symmetry plane. With increasing carrier-gas fraction, the two distinct peaks merge into one and the rest of the profile is more curved. All velocity profiles depict two broad peaks and a trough at the symmetry, but with higher carrier-gas fraction  $y_{He}$ , the velocity magnitude significantly increases [Fig. 5(c)]. The normalized silver number deposition profile, which is the product of the normalized number density and the velocity (divided by the silver inlet velocity), i.e.,  $\dot{n}_{Ag}/\dot{n}_{Ag,in} = (n_{Ag}u_{Ag})/(n_{Ag,in}u_{Ag,in})$ , is shown in Fig. 5(e). It increases nearly linearly from the outer side toward its peaks

and shows a considerable trough in between for the pure silver mixture. With increasing helium mole fraction, the profile becomes curved and broad peaks are visible around the inlet positions and one or two peaks occur at or next to the symmetry plane. The velocity trough at the symmetry trenches a deposition trough for the low carrier-gas fractions and compensates for the number density peak for high carrier-gas fractions, thus smoothing the deposition profile. This explains the smaller non-uniformity when adding high carrier-gas fractions. At higher nozzle-to-plate distance of  $x = 15$  mm, the number density is pluglike for small carrier-gas fractions  $y_{He}$  and forms a triangle profile with a high peak for high  $y_{He}$  [Fig. 5(b)]. The velocity profiles [Fig. 5(d)] flatten out producing a deposition profile, which



strongly resembles the number density profile. With higher helium fraction, the peaks merge into one narrow high peak, which explains the increase of nonuniformity with carrier-gas fraction above  $y_{\text{He}} = 0.7$  previously observed in Fig. 3(b).

The underlying flow behavior can be split into two phenomena to understand the effect of the carrier gas, namely,

1. species separation due to rarefaction, and subsequent change of the speed of sound with molecular weight,
2. subsequent change of  $\Gamma^+$ - and  $\Gamma^-$ -characteristics.

While the species separation requires rarefied flow conditions, since it is proportional to the mean free path, the definition of speed of sound and the characteristics make sense only in (near) continuum flows—as observed in the shock and at the beginning of the expansions.

### A. Free molecular flow

To visualize phenomenon 1, we consider the extreme case of free molecular flow ( $Kn \rightarrow \infty$ ) where species separation is purely based on the difference of the velocity standard deviations. Figure 6 plots free molecular flow of two parallel plumes, each of them has a carrier-gas fraction of  $y_{\text{He}} = 0.5$ . At the inlet, silver and helium are in equilibrium, i.e.,  $T_{\text{Ag}} = T_{\text{He}}$ . The variance of the velocity distributions is  $k_B T/m$ , so that silver has a narrower velocity distribution than helium, which affects the spreading of the species. Figure 6(a) shows the emerging number density field for silver in the upper and helium in the lower half, respectively. The silver number density decreases with distance from the inlet, mildly along the jet axis and more rapidly in the offside, producing isocontours in the form of ellipses. In contrast, for the lighter helium, the number density decreases rapidly in all directions causing nearly circular isocontours. The mean velocity of the mixture in x-direction [in the upper half of Fig. 6(b)] increases with distance to the inlet and takes values around  $900 \text{ m s}^{-1}$ , whereas the one in z-direction is highest in the peripheral regions [shown in the lower half of Fig. 6(b)]. Figure 6(c) shows the slip velocity of helium  $\Delta u = u_{\text{He}} - u$ , which qualitatively resembles the mean velocity field, but helium exceeds the mean velocities of the mixture by two to three times in both x- and z-direction. Figure 6(d) plots the resulting species separation ratio, i.e., the species ratio compared to the species ratio at the inlet,

$$\chi = \frac{n_{\text{Ag}}/n_{\text{He}}}{n_{\text{Ag},in}/n_{\text{He},in}}.$$

The upper half shows the DSMC solution for the mixture; the lower half shows the analytical solution given by Cai *et al.*,<sup>52,53</sup> which describes the entire flow field for a planar plume as a function of the speed ratio at the inlet  $S_{in} = U_{in}/\sqrt{2k_B T/m}$ . It can be seen that the DSMC results are in good agreement with the analytical solution. The species separation ratio is above unity in most regions indicating the predominance of silver especially around the jet axes, whereas helium prevails only in the peripheral region. Silver, the heavy species, which exhibits moderate speeds, has a higher number density fraction along the jet axis, whereas the light helium swiftly leaves the computational domain.

Farther downstream, the superposition of the two plumes produces an even higher fraction of silver around the symmetry plane. On the one hand, this behavior explains the small stray deposition of silver in Figs. 4(a) and 4(b). On the other hand, the prevalence of silver and its high molecular weight lets it dominate other flow fields, such as the temperature (and consequently the local speed of sound).

### B. Rarefied flow field

When considering collisions, the high slip velocities between silver and helium diminish. The contours in Fig. 7 compare the flow fields for the case for  $y_{\text{He}} = 0.1$  in the upper half with the case for  $y_{\text{He}} = 0.9$  in the lower half, both for  $Kn = 2Kn_0$ . The normalized number density [Fig. 7(a)] decreases in the primary expansion but increases around the symmetry plane further downstream before expanding again. The interaction shock is expected to lie between the primary and secondary expansion. For the higher carrier-gas fraction, the entire structure is elongated, which indicates that the helium focuses the heavy silver first around the primary jet axis—producing a shock further downstream—and then around the secondary jet axis, i.e., symmetry plane. Figure 7(b) shows the slip velocity of helium in x-direction. Please note that high gradients at some edges of the computational domain can be accounted to the vacuum boundary condition and the higher scattering for  $y_{\text{He}} = 0.1$  comes from the lower number of helium particles. The slip velocity is an order of magnitude smaller than in the case of free flow [upper half of Fig. 6(c)] but still positive in the majority of the flow field. In the shock region, the slip velocity is smaller and for  $y_{\text{He}} = 0.9$  even partially negative, which indicates an earlier shock of the lighter species. Figure 7(c) plots the slip velocity of helium in z-direction. The helium escapes in both directions away from the jet axis downstream of the inlet as for the free molecular flow. The z-velocity slip increases in the shock region and is everywhere directed away from the symmetry plane in the secondary expansion. An especially high local slip  $\Delta w_{\text{He}}$  can be found in the shock region for  $y_{\text{He}} = 0.9$ , which coincidences with the negative streamwise slip velocity  $\Delta u_{\text{He}}$ . Both indicate that the light helium is ejected out of the shock region by the collisions with the heavy silver.

The resulting species separation ratio [Fig. 7(d)] is in most regions above unity as was already the case for free molecular flow. However, in the shock region, the smaller or even reversed helium slip velocities compared to the free molecular case cause a dip in species separation. For higher carrier-gas fraction, the species separation is stronger in the expansions but also the zone of less species separation around the shock is larger, which is in agreement with the higher impact of the shock region on the slip velocities. The prevalence of silver comes along with a higher local mass, thus (given a certain temperature) a smaller standard deviation of fluctuational velocities and, hence, a lower speed of sound, which varies with  $a \propto \sqrt{T/m}$ . The factors with which local weight and temperature alter the speed of sound can be separated. Figure 7(e) plots the factor due to the change of local weight, which is the square root of the inverse of the molecular mass normalized by the inlet molecular mass, i.e.,  $\sqrt{m_{in}/m}$ . This factor is close to unity for the majority of the flow field for  $y_{\text{He}} = 0.1$  implying negligible impact of species separation on the speed of sound, except for the

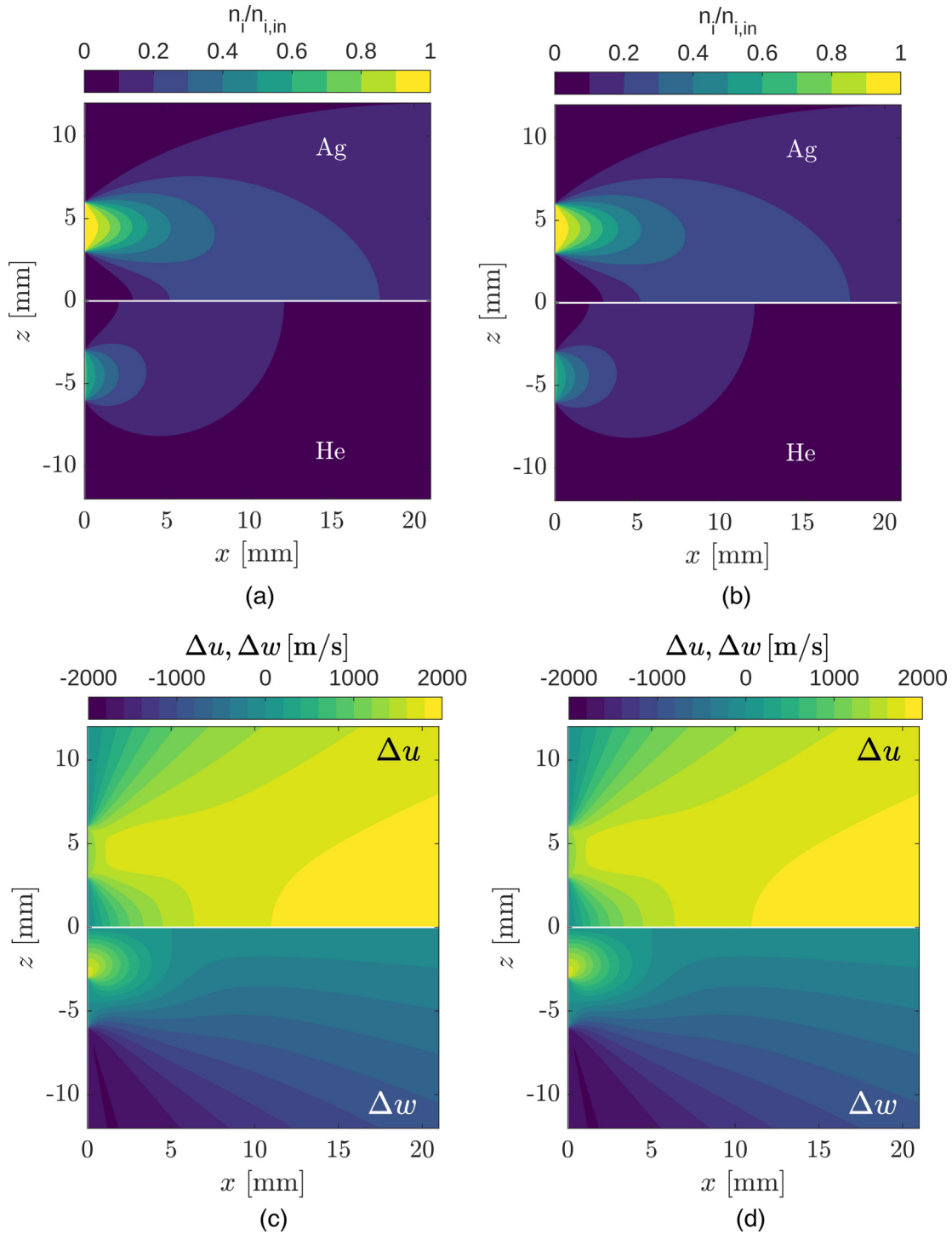


**FIG. 6.** Contours of free molecular flow of two interacting plumes of a homogeneous binary gas mixture with a carrier-gas fraction of  $\gamma = 0.5$ . (a) shows the number density of silver in the upper and the one of helium in the lower half; (b) depicts the mean velocity of the mixture and (c) the slip velocity of helium, in the upper half is the  $x$ -component, in the lower half the  $z$ -component; (d) presents the species separation ratio  $\chi$  calculated by DSMC in the upper half and calculated from an analytical solution in the lower half.

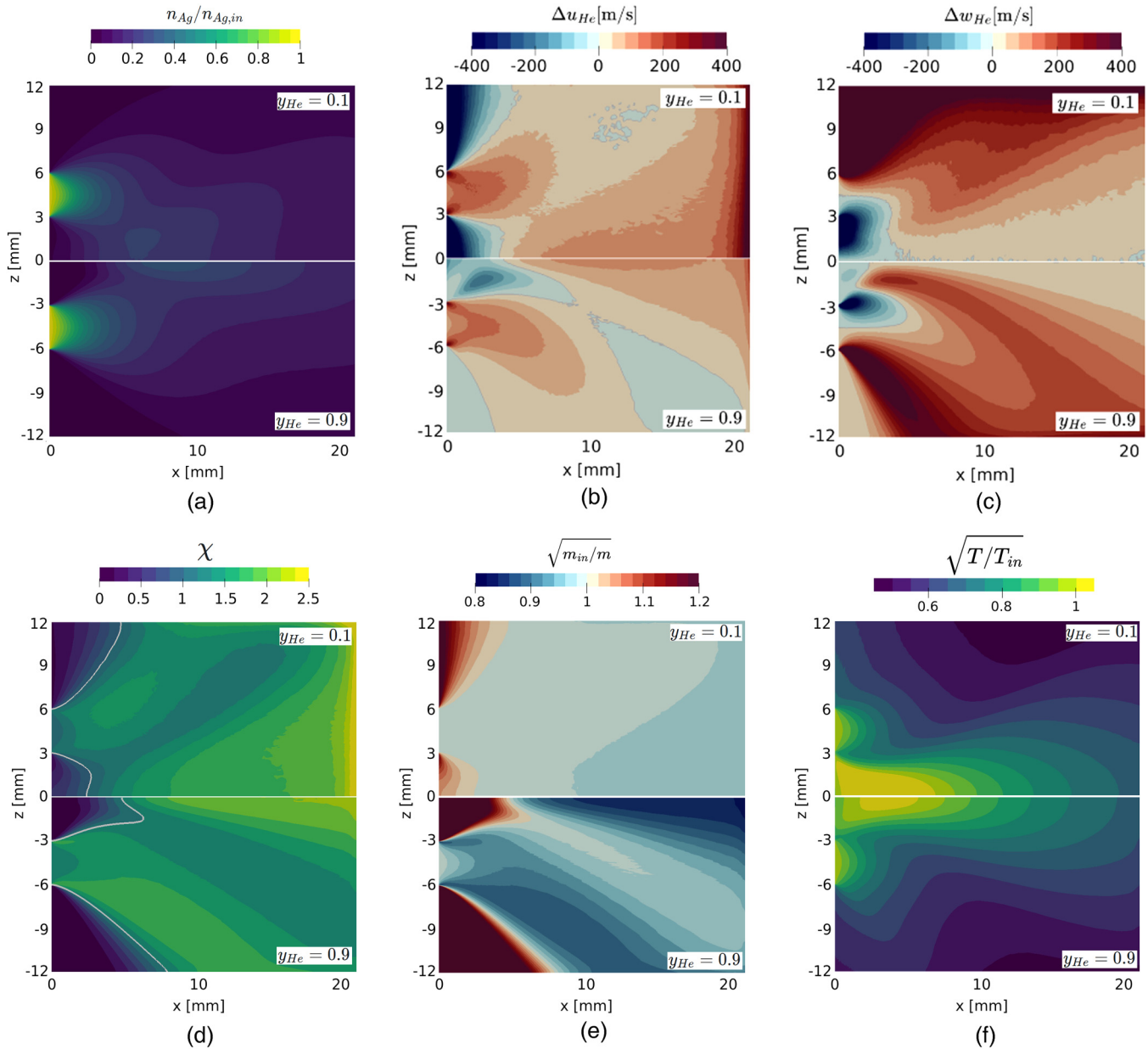


**FIG. 7.** Contour plots of two interacting jets of a binary gas mixture for  $Kn = 2Kn_0$ , in the upper half for a carrier-gas fraction of  $y_{He} = 0.1$ , in the lower half for a carrier-gas fraction of  $y_{He} = 0.9$ . (a) shows the silver number density normalized by the inlet silver number density, (b) the helium slip velocity in x-direction, (c) the helium slip velocity in z-direction, (d) the species separation ratio  $\chi$  where the gray line marks  $\chi = 1$ , (e) the contribution factor of molecular weight to the change of speed of sound, and (f) the contribution factor of temperature to the change of speed of sound. The contour plots are clipped to the range of the corresponding color bar.

peripheral highly rarefied regions where the factor reaches high values. For  $y_{He} = 0.9$ , the molecular mass factor is up to 14% lower in the primary expansion and rises due to the interaction at the symmetry plane (which also occurs in a pure mixture case). Differences due to species separation are noticeable when comparing the cases of different carrier-gas fractions. However, these mainly occur in the highly

separation is directly reflected in a molecular mass factor that deviates from unity, the temperature factor mainly drops due to the expansion and rises due to the interaction at the symmetry plane (which also occurs in a pure mixture case). Differences due to species separation are noticeable when comparing the cases of different carrier-gas fractions. However, these mainly occur in the highly

rarefied regions, e.g., the peripheral region above the inlet and the early interaction region with high temperatures. In these almost free molecular flow regions, the definition of the speed of sound is pointless. In the core of the expansions and in the shock region, the temperature factor exhibits symmetrical behavior for  $y_{\text{He}} = 0.1$  and  $y_{\text{He}} = 0.9$ . Hence, it can be concluded that the speed of sound changes because of the change in local molecular mass due to species separation (and changes in temperature are not relevant).

An explanatory remark regarding the change of the speed of sound and the species separation ratio: We chose the species separation ratio  $\chi$  as a measure commonly used in literature.<sup>45</sup> One should keep in mind that for the same species separation ratio the change in local mean molecular mass depends on the initial carrier-gas fractions, e.g., for  $\chi = 2$  the molecular mass changes more for  $y_{\text{He},in} = 0.9$  than  $y_{\text{He},in} = 0.1$ . The expression reads

$$\frac{m}{m_{in}} = \frac{1 + r_{in}}{1 + \chi r_{in}} \frac{m_{\text{He}} + \chi r_{in} m_{\text{Ag}}}{m_{\text{He}} + r_{in} m_{\text{Ag}}},$$

where  $r_{in} = n_{\text{Ag},in}/n_{\text{He},in} = (1 - y_{\text{He},in})/y_{\text{He},in}$  is the species ratio at the inlet, which is  $r_{in} = 9$  for  $y_{\text{He},in} = 0.1$  and  $r_{in} = 1/9$  for  $y_{\text{He},in} = 0.9$ .

### C. Change of $\Gamma^+$ and $\Gamma^-$ characteristics

Due to the previously described reduction of the speed of sound by the species separation, a fluid element has a narrower domain of influence, which is the Mach cone whose half-cone aperture is the Mach angle  $\mu = \arcsin(\frac{1}{M})$  that decreases for lower speeds of sound. The corresponding envelopes are the  $\Gamma^+$ - and  $\Gamma^-$ -characteristics so that the impact of local species separation on the flow field can be visualized by these characteristics. The course of the characteristics  $\Gamma^+$  and  $\Gamma^-$  can be expressed by the local flow angle  $\varphi$  and the Mach angle  $\mu$  and reads

$$\Gamma^+ : \frac{dz}{dx} = \tan(\varphi + \mu), \quad (6)$$

$$\Gamma^- : \frac{dz}{dx} = \tan(\varphi - \mu). \quad (7)$$

Please note that the description by characteristics is only strictly applicable for inviscid continuum flow and in the here considered rarefied flow, it aids the understanding since the deviation from equilibrium is small. For more details on the characteristics of supersonic, inviscid continuum flows refer to the literature.<sup>54</sup>

Figure 8 plots the Mach number field as banded contours, streamlines in blue, and characteristic curves in brown and beige. The case for a carrier-gas fraction of  $y_{\text{He}} = 0.1$  is shown in the upper half and the one for  $y_{\text{He}} = 0.9$  in the lower half. In both cases, the Mach number increases in the primary expansion, decreases when crossing the shock, and again increases in the secondary expansion. For the high carrier-gas fraction, the Mach number increases faster—since the stronger species separation cumulates the heavy silver as was shown in Fig. 7—and, therefore, the characteristics form a more acute angle with the streamline. This narrower expansion affects the shock location. The shock region is detected

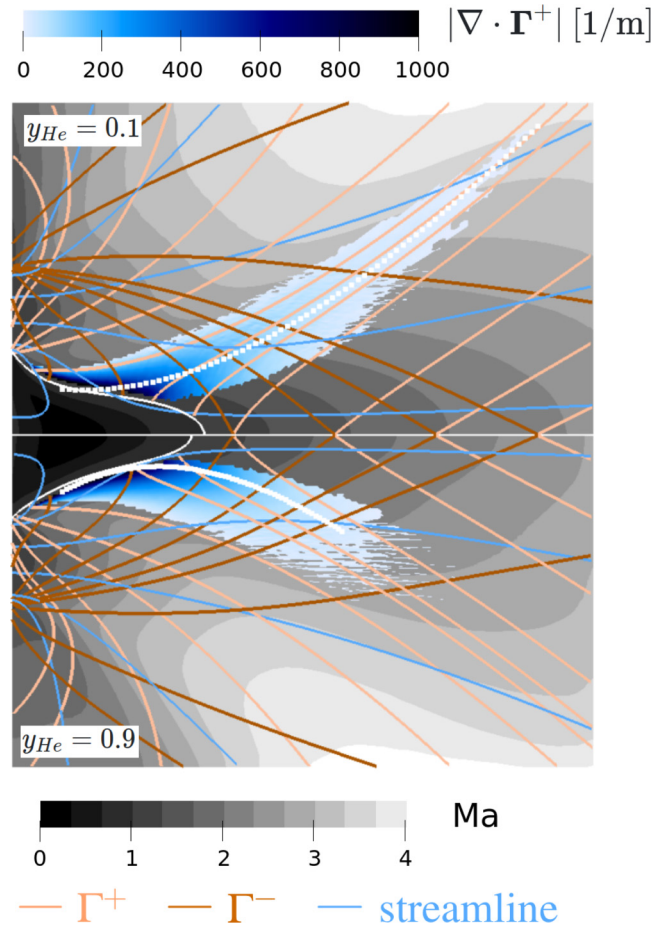


**FIG. 8.** Characteristics and shock detection for  $y_{\text{He}} = 0.1$  in the upper half and  $y_{\text{He}} = 0.9$  in the lower half at inlet Knudsen number  $Kn = 2Kn_0$ . The gray, banded contours in the background show the Mach number and the blue, continuous contours represent the region detected as the shock region and are colored by  $|\nabla \cdot \Gamma^+|$ , clipped at  $1000 \text{ m}^{-1}$ . The blue lines are streamlines, the brown lines  $\Gamma^-$  characteristics, and the beige lines  $\Gamma^+$  characteristics (in the lower part the characteristics are mirrored). The white dotted line is the shock line detected from the regression of the shock region; the white solid line is the sonic line, i.e.,  $M = 1$ .

based on the divergence field of the  $\Gamma^+$ -characteristics and marked by the blue continuous contours. While the shock region traverses nearly the entire computational domain for  $y_{\text{He}} = 0.1$ , it fades early for  $y_{\text{He}} = 0.9$  and bends away less from the symmetry plane. (Details of the shock detection method were described in a previous publication.<sup>20</sup> Its benefit over the commonly used isobars<sup>55</sup> or pseudo-Schlieren<sup>56</sup> is that it does not lose its validity when the preshock condition is highly inhomogeneous in pressure and density along the shock, which is the case in the present study due to the expansion flow.)

Figure 9 plots the shock location and sonic line for different carrier-gas fractions for  $Kn = Kn_0$  and  $Kn = 2Kn_0$ . The subsonic region (marked by solid lines) changes only insignificantly with



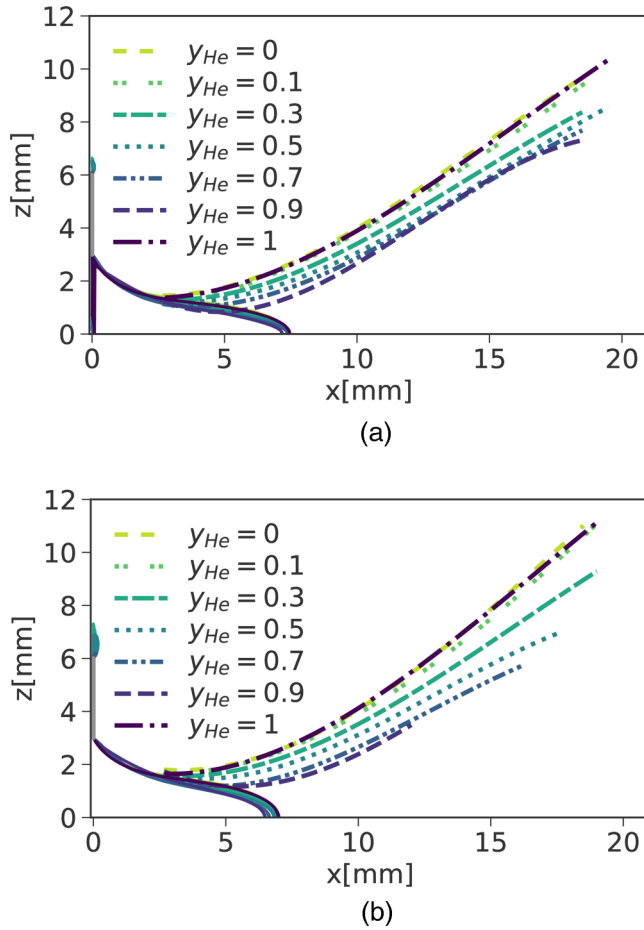


**FIG. 9.** Shock location (dashed or dotted) and sonic line (solid) depending on the carrier-gas fraction for (a)  $Kn = Kn_0$  and (b)  $Kn = 2Kn_0$ .

carrier-gas fraction. For pure helium and pure silver the shock location matches—which is expected due to similarity that depends only on the Mach number and marginally on the Knudsen number,<sup>20</sup> which were kept the same for all cases. A small carrier-gas fraction of  $y_{He} = 0.1$  has only a negligible impact on the shock location. However, the shock location shifts downstream for higher carrier-gas fractions and the divergence region becomes shorter so that the shock does not traverse through the entire domain but diffuses before. This greater deviation corresponds to the higher change of local mean molecular mass due to species separation. Hence, the information that an interaction takes place cannot travel as far upstream, producing a later shock. In addition, the shock region is broader and weaker for the higher carrier-gas fraction, which can be accounted to a more oblique shock due to the shift. The shift of the shock and its weakening is more prominent for a higher degree of rarefaction, i.e.,  $Kn = 2Kn_0$  in Fig. 9(a), since for longer mean free paths atoms can move a longer distance without collisions thus enhancing species separation.<sup>57</sup> The narrower shock

region and weaker shock explain the smaller distance between peaks and smaller peak height observed in the deposition profiles for high carrier-gas fractions. The fading of the shocks reveals why at high carrier-gas fractions and rarefaction, the deposition profile seems to resemble the merging of the two plumes [Fig. 5(f)] and consequently produces a higher nonuniformity than at lower carrier-gas fractions [Fig. 3(b)].

#### IV. CONCLUSIONS

We investigated the use of a light carrier gas to support continuous physical vapor deposition (PVD) processes of a heavier species, in which plume interactions (otherwise) would cause shocks. To evaluate the effect of species separation, we kept the Mach number and the Knudsen number constant while varying the carrier-gas fraction.

At the inlet, the addition of a carrier gas increases the speed of sound and consequently the mass flow of the coating material from a sonic inlet. In the expansion flow, a higher carrier-gas fraction produces a stronger separation of species that pushes the light species to the offside and focuses the heavy species along the axis. Consequently, stray deposition reduces monotonically with carrier-gas fraction. In the region with a high fraction of heavy species, the Mach number increases more compared to cases with lower carrier-gas fractions. This shifts the transfer of information into a smaller Mach cone, which in turn produces a less bent and more oblique, weaker shock. Therefore, the impact of the shock on the deposition profile is reduced. This improves deposition uniformity up to the point at which adding more carrier gas causes a merging of the two plumes into one and uniformity decreases. A higher rarefaction enhances the merging of the plumes.

Thus, the three main requirements concerning the mass flow—high mass flow rates, low stray deposition, and high uniformity—are all facilitated by adding a lighter carrier gas (up to a certain carrier-gas fraction). While we showed these beneficial outcomes only for planar plume interaction with a very specific geometry, the same effects can be expected for other nozzle geometries and three-dimensional interacting plumes. A simplification made in the current study is that the influence of the actual substrate is not considered. The applied vacuum condition removes the gases and does not allow backflow. For the applied metal, i.e., silver, this is may be an appropriate assumption since the majority of it is expected to stick on the substrate surface. The carrier gas, i.e., helium, rebounds from the substrate and may affect the upstream flow. Further studies (with the precise geometry) would be necessary to evaluate this effect. The carrier gases will not only impact the transport to the substrate but also the growth of the film. The exact effect depends on the deposited material, process conditions, and desired film morphology. Experiments would be required for a comprehensive evaluation of carrier gas use in continuous PVD.

#### Nomenclature

##### Roman symbols

- $a = \sqrt{\gamma RT}$  speed of sound ( $\text{m s}^{-1}$ )
- $D$  = length of inlet (m)
- $d$  = collisional diameter (m)
- $k_B$  = Boltzmann constant ( $1.380\,649 \times 10^{-23} \text{ J K}^{-1}$ )

$Kn$  = Knudsen number (–)  
 $L$  = nozzle separation distance (m)  
 $M$  = Mach number (–)  
 $m$  = particle mass (kg)  
 $n$  = number density ( $\text{m}^{-3}$ )  
 $p_{\text{loss}}$  = fraction of loss deposition (–)  
 $R$  = specific gas constant ( $\text{J kg}^{-1} \text{K}^{-1}$ )  
 $\mathbf{r}$  =  $(x, z)$  point vector (m)  
 $S$  = speed ratio (–)  
 $T$  = temperature (K)  
 $\mathbf{u} = (u, w)$  macroscopic velocity ( $\text{m s}^{-1}$ )  
 $y$  = mole fraction (–)

#### Greek

$\alpha$  = deflection angle exponent (–)  
 $\chi$  = species separation ratio (–)  
 $\gamma$  = specific heat ratio  
 $\Gamma^+, \Gamma^-$  = characteristics  
 $\lambda$  = mean free path (m)  
 $\mu$  = Mach angle ( $^\circ$ )  
 $\omega$  = energy exponent (–)  
 $\rho$  = density ( $\text{kg m}^{-3}$ )  
 $\varphi$  = flow angle ( $^\circ$ )

#### Subscripts

Ag = silver  
 He = helium  
 in = quantity at the inlet  
 ref = reference value

#### ACKNOWLEDGMENTS

J. E. Vesper would like to thank Luis Portela for an insightful discussion on species separation. This research was carried out under Project No. F22.3.13512 within the framework of the Industrial Partnership Program of the Materials innovation institute M2i ([www.m2i.nl](http://www.m2i.nl)) and the Foundation for Fundamental Research on Matter (FOM), which is part of the Dutch Research Council (NWO).

#### AUTHOR DECLARATIONS

##### Conflict of Interest

The authors have no conflicts to disclose.

#### DATA AVAILABILITY

The data that support the findings of this study are available from the corresponding author upon reasonable request.

#### APPENDIX: TIME STEP, MESH, AND PARTICLE NUMBER INDEPENDENCE STUDY

The independence of the solution was tested exemplary for the case  $Kn = 2Kn_0 = 0.025$  and  $y_{\text{He}} = 0.5$ . The results in the manuscript were drawn from a simulation containing a number of particles of  $N_p = 3.27M$ , a time step of  $dt_0 = 2.5 \times 10^{-9} \text{ s}$  and a number of cells of  $N_c = 56\,784$ . This corresponds to fulfilling the resolution criteria for time step  $dt < \tau/10$ , grid size  $dx < 2\lambda/3$  everywhere and particle number per cell being at least 20 as

described in Sec. II. The resolution was varied to study the independence of the solution on the discretization. The silver number density flux normalized by the silver inlet number density flux at a nozzle-to-plate distance of  $x = 8 \text{ mm}$  is plotted for the different resolutions in Fig. 10. The time step was varied with  $dt \in [0.5dt_0, dt_0, 2dt_0, 10dt_0, 40dt_0, 100dt_0]$ . For a time step size of  $dt = 40dt_0$  and  $dt = 100dt_0$ , the predicted normalized number density flux varies from the one at smaller time step sizes, whereas the deviations for  $dt \in [0.5dt_0, dt_0, 2dt_0, 10dt_0]$  are small to negligible [Fig. 10(a)]. The grid cell size was refined by a factor of 2,

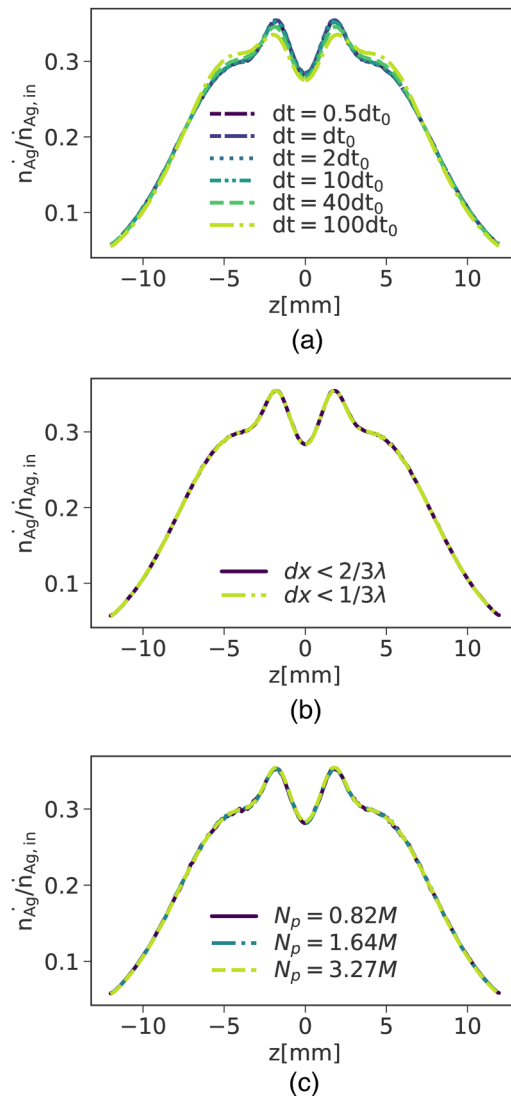


**FIG. 10.** Independence study for interacting plumes at  $Kn = 2Kn_0 = 0.025$  and  $y_{\text{He}} = 0.5$ . Line plot of the silver number density flux normalized by the silver inlet number density flux at a nozzle-to-plate distance of  $x = 8 \text{ mm}$  for (a) varying time step sizes, (b) varying mesh size, and (c) varying particle number.

increasing the number of cells by a factor 4 so that the mesh globally fulfilled  $dx < 1\lambda/3$ . The particle number was adapted to keep the number of particles per cell constant. The resulting number density fluxes match for the different grid refinements [Fig. 10(b)]. The particle number was varied to be 0.25 and 0.5 of the standard particle number. The results for the different particle numbers match each other [Fig. 10(c)]. Based on these good results for the chosen resolution, we expect the fulfillment of the previously discussed and widely referenced resolution criteria to be sufficient for a discretization refinement independent solution. The actual time step size, grid, and number of particles were adapted for each case individually to ensure the fulfillment of the criteria.

## REFERENCES

- <sup>1</sup>H. Liu, Y. Zhu, Q. Meng, X. Lu, S. Kong, Z. Huang, P. Jiang, and X. Bao, *Nano Res.* **10**, 643 (2017).
- <sup>2</sup>A. Drize and A. Settaouti, *Ind. J. Pure Appl. Phys.* **56**, 434 (2018).
- <sup>3</sup>A. Torgovkin, S. Chaudhuri, A. Ruhtinas, M. Lahtinen, T. Sajavaara, and I. Maasilta, *Supercond. Sci. Technol.* **31**, 055017 (2018).
- <sup>4</sup>R. Dorsman, C. Kleijn, J. Velthuis, J. Zijp, and A. van Mol, *J. Vac. Sci. Technol. A* **25**, 474 (2007).
- <sup>5</sup>K. Bobzin, R. P. Brinkmann, T. Mussenbrock, N. Bagcivan, R. H. Brugnara, M. Schäfer, and J. Trieschmann, *Surf. Coat. Technol.* **237**, 176 (2013).
- <sup>6</sup>M. C. Schwillie, T. Schössler, J. Barth, M. Knaut, F. Schön, A. Höchst, M. Oettel, and J. W. Bartha, *J. Vac. Sci. Technol. A* **35**, 01B118 (2017).
- <sup>7</sup>S. Thirupathiraj, S.-M. Ryu, J. Uh, and L. L. Raja, *J. Vac. Sci. Technol. A* **39**, 052404 (2021).
- <sup>8</sup>J. F. Groves, S. Jones, T. Globus, L. Hsiung, and H. Wadley, *J. Electrochem. Soc.* **142**, L173 (1995).
- <sup>9</sup>D. D. Hass and B. Gogia, U.S. patent App. 13/178, 135 (2013).
- <sup>10</sup>A. Moarrefzadeh and M. Branch, *WSEAS Trans. Appl. Theor. Mech.* **7**, 106 (2012).
- <sup>11</sup>T. M. Rodgers, H. Zhao, and H. N. Wadley, *J. Vac. Sci. Technol. A* **33**, 05E118 (2015).
- <sup>12</sup>T. M. Rodgers, H. Zhao, and H. N. Wadley, *J. Vac. Sci. Technol. A* **33**, 061509 (2015).
- <sup>13</sup>N. Bykov and V. Zakharov, *Phys. Fluids* **32**, 067109 (2020).
- <sup>14</sup>N. Wei, Y. Feng, W. Sun, Y. Cheng, M. Dong, Y. Song, C. Wu, G. Liu, and Y. Qiu, *Vacuum* **189**, 110277 (2021).
- <sup>15</sup>E. Zoestbergen, T. Maalman, C. Commandeur, and M. Goodenough, *Surf. Coat. Technol.* **218**, 108 (2013).
- <sup>16</sup>J. E. Vesper, C. S. Obiji, R. Westerwaal, C. Boelsma, S. Kenjereš, and C. R. Kleijn, *Appl. Therm. Eng.* **195**, 117099 (2021).
- <sup>17</sup>P. Banaszak, D. Marneffe, E. Silberberg, and L. Vanhee, "Industrial vapour generator for the deposition of an alloy coating onto a metal strip," US Patent App., 12/681, 969 (Google Patents, 2011).
- <sup>18</sup>A. Venkatraman and A. A. Alexeenko, *Vacuum* **86**, 1748 (2012).
- <sup>19</sup>A. Venkatraman and A. A. Alexeenko, *J. Vac. Sci. Technol. A* **28**, 916 (2010).
- <sup>20</sup>J. E. Vesper, T. J. Broeders, J. Batenburg, D. E. van Odyck, and C. R. Kleijn, *Phys. Fluids* **33**, 086103 (2021).
- <sup>21</sup>T. Dutta, K. Sinhamahapatra, and S. Bandyopadhyay, *Int. J. Refrig.* **34**, 2118 (2011).
- <sup>22</sup>S. Mohammadi and F. Farhadi, *Sep. Purif. Technol.* **138**, 177 (2014).
- <sup>23</sup>J. Yun, Y. Kim, and S. Yu, *Int. J. Heat Mass Transfer* **126**, 353 (2018).
- <sup>24</sup>S. Kuwatani, S. Watanabe, and N. Ono, *J. Therm. Sci. Technol.* **7**, 31 (2012).
- <sup>25</sup>T. Saiki, N. Ono, S. Matsumoto, and S. Watanabe, *Int. J. Heat Mass Transfer* **163**, 120394 (2020).
- <sup>26</sup>M. Sabouri and M. Darbandi, *Phys. Fluids* **31**, 042004 (2019).
- <sup>27</sup>T. Wu and A. Firoozabadi, *J. Phys. Chem. C* **122**, 20727 (2018).
- <sup>28</sup>A. D. Strongrich, A. J. Pikus, I. B. Sebastiao, D. Peroulis, and A. A. Alexeenko, "Low-pressure gas sensor exploiting the Knudsen thermal force: DSMC modeling and experimental validation," in *2016 IEEE 29th International Conference on Micro Electro Mechanical Systems (MEMS)* (IEEE, Shanghai, China, 2016), pp. 828–831.
- <sup>29</sup>R. Gatignol and C. Croizet, *Phys. Fluids* **29**, 042001 (2017).
- <sup>30</sup>A. Lotfian and E. Roohi, *Int. Commun. Heat Mass Transfer* **121**, 105061 (2021).
- <sup>31</sup>H. Sugimoto, S. Takata, and S. Kosuge, *Rarefied Gas Dyn.* **1**, 1158 (2007).
- <sup>32</sup>S. Takata, H. Sugimoto, and S. Kosuge, *Eur. J. Mech. B* **26**, 155 (2007).
- <sup>33</sup>S. Nakaye and H. Sugimoto, *Vacuum* **125**, 154 (2016).
- <sup>34</sup>H. Trinks, "Gas species separation effects in exhaust plumes," in *5th Joint Thermophysics and Heat Transfer Conference* (AIAA, Reston, VA, 1990), p. 1734.
- <sup>35</sup>K. H. Lee, *PLoS One* **12**, e0176423 (2017).
- <sup>36</sup>K. H. Lee, *Comput. Fluids* **173**, 259 (2018).
- <sup>37</sup>F. S. Sherman, *Phys. Fluids* **8**, 773 (1965).
- <sup>38</sup>D. E. Rothe, *Phys. Fluids* **9**, 1643 (1966).
- <sup>39</sup>A. Ramos, G. Tejada, J. Fernández, and S. Montero, *J. Phys. Chem. A* **113**, 8506 (2009).
- <sup>40</sup>V. V. Riabov, *J. Thermophys. Heat Transfer* **17**, 526 (2003).
- <sup>41</sup>V. Kosyanchuk and A. Yakunchikov, *Phys. Fluids* **33**, 082007 (2021).
- <sup>42</sup>J. Wu, G. Cai, B. He, and H. Zhou, *Vacuum* **128**, 166 (2016).
- <sup>43</sup>D. E. Rothe, Technical Report (Institute for Aerospace Studies, Toronto University, Ontario, 1966).
- <sup>44</sup>A. Ramos, G. Tejada, J. Fernández, and S. Montero, *J. Phys. Chem. A* **114**, 7761 (2010).
- <sup>45</sup>G. Bird, *Molecular Gas Dynamics and the Direct Simulation of Gas Flows* (Oxford University Press, Oxford, 1994).
- <sup>46</sup>K. Koura and H. Matsumoto, *Phys. Fluids A* **4**, 1083 (1992).
- <sup>47</sup>J. Fan, I. D. Boyd, and C. Shelton, *J. Vac. Sci. Technol. A* **18**, 2937 (2000).
- <sup>48</sup>P. Fialho, J. Fareira, M. Ramires, and C. A. Nieto de Castro, *Ber. Bunsenges. Phys. Chem.* **97**, 1487 (1993).
- <sup>49</sup>E. Roohi and S. Stefanov, *Phys. Rep.* **656**, 1 (2016).
- <sup>50</sup>C. White, M. K. Borg, T. J. Scanlon, S. M. Longshaw, B. John, D. Emerson, and J. M. Reese, *Comput. Phys. Commun.* **224**, 22 (2018).
- <sup>51</sup>D. Valougeorgis, M. Vargas, and S. Naris, *Vacuum* **128**, 1 (2016).
- <sup>52</sup>C. Cai and I. D. Boyd, *J. Spacecr. Rockets* **44**, 619 (2007).
- <sup>53</sup>S. Cai, C. Cai, and J. Li, *Phys. Fluids* **30**, 127101 (2018).
- <sup>54</sup>R. Vos and S. Farokhi, *Introduction to Transonic Aerodynamics* (Springer, Dordrecht, The Netherlands, 2015), Vol. 110.
- <sup>55</sup>I. W. Kokkinakis, D. Drikakis, K. Ritos, and S. M. Spottswood, *Phys. Fluids* **32**, 066107 (2020).
- <sup>56</sup>O. Tumuklu and D. A. Levin, "On the temporal evolution in laminar separated boundary layer shock-interaction flows using DSMC," in *55th AIAA Aerospace Sciences Meeting* (AIAA, Reston, VA, 2017), p. 1614.
- <sup>57</sup>S. Chapman, *Proc. Roy. Soc. Lond. A* **93**, 1 (1916).